Applied Physics Letters

RESEARCH ARTICLE | SEPTEMBER 02 2022

Spin-generation in magnetic Weyl semimetal Co_2MnGa across varying degree of chemical order

Taqiyyah S. Safi ; Chung-Tao Chou ; Justin T. Hou; Jiahao Han ; Luqiao Liu

Appl. Phys. Lett. 121, 092404 (2022)
https://doi.org/10.1063/5.0102039

AIP Publishing

Applied Physics Letters ARTICLE scitation.org/journal/apl

Spin-generation in magnetic Weyl semimetal Co_2MnGa across varying degree of chemical order

Cite as: Appl. Phys. Lett. **121**, 092404 (2022); doi: 10.1063/5.0102039
Submitted: 6 June 2022 · Accepted: 14 August 2022 ·
Published Online: 2 September 2022

Taqiyyah S. Safi,[1,a)] Chung-Tao Chou,[2] Justin T. Hou,[1] Jiahao Han,[1] and Luqiao Liu[1]

AFFILIATIONS

[1]Department of Electrical Engineering and Computer Science, Massachusetts Institute of Technology, Cambridge, Massachusetts 02139, USA
[2]Department of Physics, Massachusetts Institute of Technology, Cambridge, Massachusetts 02139, USA

[a)]Author to whom correspondence should be addressed: tsafi@mit.edu

ABSTRACT

Recently discovered magnetic Weyl semimetals (MWSM), with enhanced Berry curvature stemming from the topology of their electronic band structure, have gained much interest for spintronics applications. In this category, Co_2MnGa, a room temperature ferromagnetic Heusler alloy, has garnered special interest as a promising material for topologically driven spintronic applications. However, until now, the structural-order dependence of spin current generation efficiency through the spin Hall effect has not been fully explored in this material. In this paper, we study the evolution of magnetic and transport properties of Co_2MnGa thin films from the chemically disordered $B2$ to ordered $L2_1$ phase. We also report on the change in spin generation efficiency across these different phases, using heterostructures of Co_2MnGa and ferrimagnet Co_xTb_{1-x} with perpendicular magnetic anisotropy. We measured large spin Hall angles in both the $B2$ and $L2_1$ phases, and within our experimental limits, we did not observe the advantage brought by the MWSM ordering in generating a strong spin Hall angle over the disordered phases, which suggests more complicated mechanisms over the intrinsic, Weyl-band structure-determined spin Hall effect in these material stacks.

In Weyl semimetals, the linearly dispersive band crossing in the three-dimensional (3D) momentum space near the Fermi energy at Weyl points with opposite chiralities (sink or source of the Berry curvature) is responsible for a rich variety of exotic properties such as topological Fermi arcs on the surface[1–4] and chiral anomaly effects in the bulk.[5–10] When the splitting of Weyl points is caused by the breaking of time-reversal symmetry, as in the case of magnetic Weyl semimetals (MWSM), many exciting magneto-transport properties show up thanks to the coupling between magnetism and Weyl electron physics, including anomalous Hall effect (AHE) and anomalous Nernst effect with extraordinarily large magnitude.[11–18] Among the various MWSM materials identified so far, the full Heusler ferromagnet Co_2MnGa represents a promising candidate for room temperature applications with a high Curie temperature $T_c \approx 700$ K (Ref. 18) and large spin polarization at the Fermi surface.

In addition to the fully ordered $L2_1$ phase where the topological Weyl state of Co_2MnGa has been observed, Co_2MnGa can take on a partially ordered $B2$ or a completely disordered $A2$ phase.[19–21] Thus, to fully harness the topological properties of Co_2MnGa, it is important to understand the relationship between the electronic, magnetic, and spin-generation properties of these different chemical phases. To this end, researchers have studied the evolution of electrical conductivity and anomalous Hall resistivity with atomic ordering in samples with $B2$ and $L2_1$ phases.[21–23] Furthermore, recently spin–orbit torque (SOT) induced switching has been demonstrated in Co_2MnGa with $B2$ phase,[24] and simultaneously a large spin Hall angle is also reported in $L2_1$ phase through nonlocal inverse spin Hall measurements using lateral spin valve structures.[25] However, a direct, calibrated comparison of the spin-current generation efficiencies from these different phases of Co_2MnGa is still missing.

In this paper, we systematically study the effect of growth conditions on the chemical order of the films and its subsequent effect on the electronic and magnetic properties of the films. We also study the effect of chemical disorders on the SOT generations from Co_2MnGa films by quantitatively determining the spin Hall angle in films of different phases.

Co_2MnGa (100 nm) films were grown on a MgO (100) substrate using a direct current (DC) magnetron sputtering from a commercial

TABLE I. Growth and annealing conditions for various Co_2MnGa samples.

Sample name	Deposition temperature T_{dep} (°C)	Annealing temperature T_{ann} (°C)
A	Room temperature	N/A
B	300	500
C	400	500
D	600	700

target. All films were grown at a base pressure of less than 3×10^{-7} Torr and at a working pressure of 3 mTorr at a low growth rate of 0.2 Å/s to ensure good film quality. We varied the substrate temperature and the post-annealing conditions to tune the degree of structural disorder.[21] The film growth and annealing temperatures (T_{dep} and T_{ann}) are tabulated in Table I, where all except the room temperature grown film were post annealed for an hour. Prior to the deposition, the substrates were preheated to the deposition temperature and soaked for half an hour. All samples were capped with ~5 nm of Pt at room temperature to prevent oxidation from air exposure.

We then carried out a structural analysis of the films using x-ray diffraction (XRD) and the results are shown in Figs. 1(a)–1(c). Strong reflections are observed from the planes (002) and (004) of Co_2MnGa samples deposited above room temperature as shown in the θ–2θ scan in Fig. 1(a), indicating the formation of the (001) texture with a high degree of long-range ordering. Figure 1(c) depicts the ϕ-scan measurements for the (202) peak on Co_2MnGa films grown at RT and at 600 °C, where the fourfold rotational symmetry and the comparative location of Co_2MnGa peaks to the substrate MgO (202) peaks confirm the epitaxial growth with $Co_2MnGa[110]//MgO[100]$.[21,22] Finally, we examined the (111) planes of our samples and found that all samples grown at $T_{dep} > 300$ °C had an obvious (111) peak. The degree of order for the $L2_1$ structure can be extracted from the intensity of the (111) superlattice peak.[20] We note that the intensity of (111) peak increased with growth temperature indicating increased chemical ordering [Fig. 1(b)]. The XRD measurement on the (111) and (002) peaks, therefore, shows that with the increase in T_{dep}, samples A to D transit from *B2*- to $L2_1$-dominated phase.

We performed magnetic measurements using a vibrating sample magnetometer (VSM) at room temperature. The in-plane magnetization loop in Fig. 2(a) shows that the saturation magnetization M_s increases with the deposition temperature, consistent with the

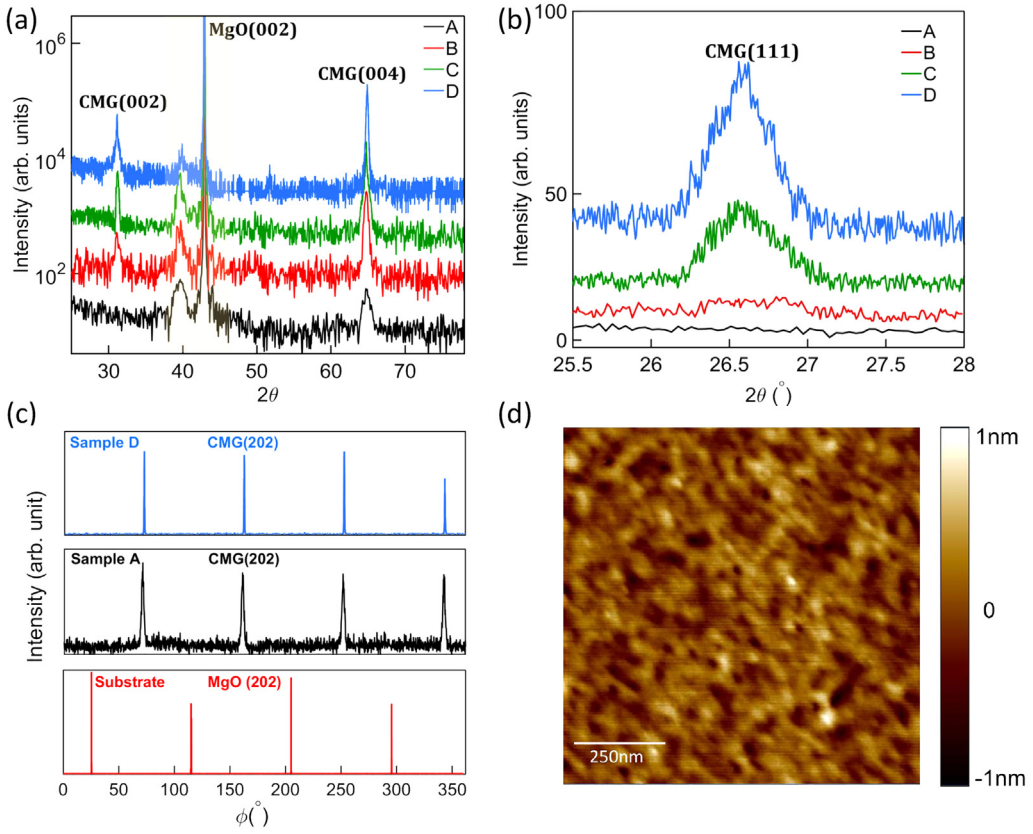

FIG. 1. (a) XRD θ–2θ scans of Co_2MnGa (100 nm) films with T_{dep} = RT, 300, 400, and 600 °C grown on the MgO (001) substrate (the shaded area depicts substrate peaks) and (b) 2θ-scan for the (111) plane and (c) ϕ-scan of (202) planes from Co_2MnGa grown at 600 °C, RT, and the MgO substrate. (d) Atomic force microscopy image of the Co_2MnGa (10 nm)/Pt (3 nm) film. The scale bar is 250 nm.

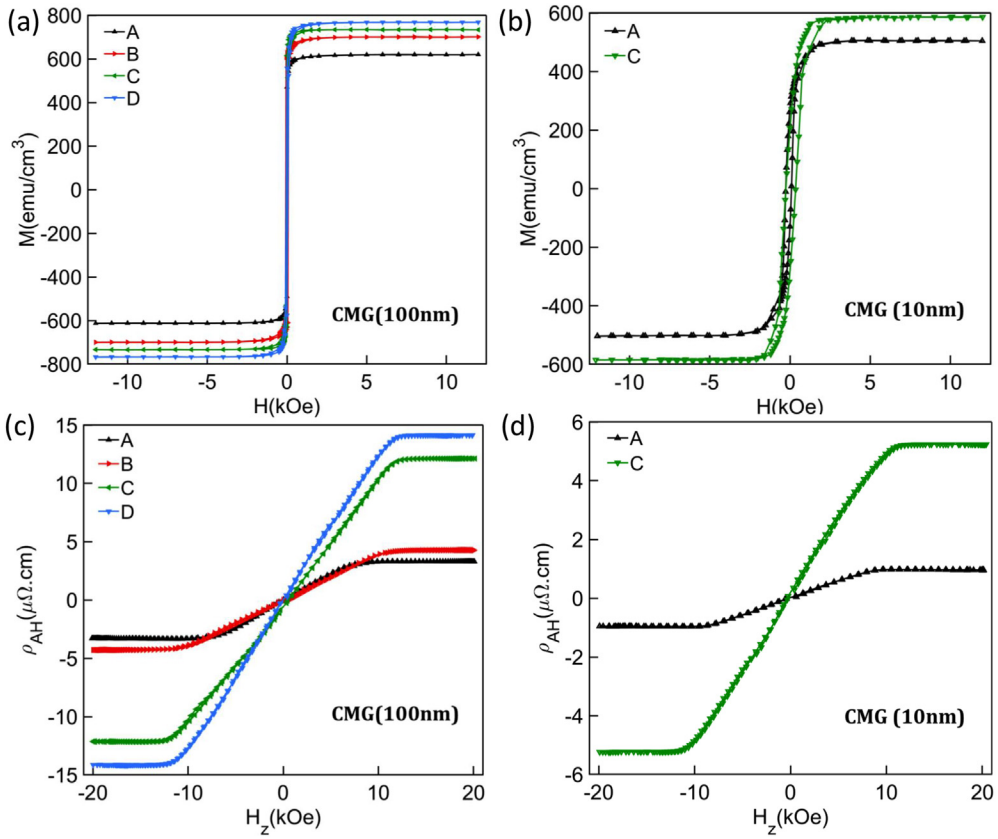

FIG. 2. In plane magnetization loops for Co_2MnGa films grown and annealed at different temperatures for (a) 100 and (b) 10 nm films. Hall resistivity as a function of applied out-of-plane field for (c) 100 and (d) 10 nm films.

previous studies[20,21] which show that an increase in the $L2_1$ phase corresponds to larger M_s. The lower M_s in the $B2$-ordered Co_2MnGa thin film is due to the antiferromagnetically coupled moment of a pair of Mn atoms.[21] At $T_{dep} = 600\,^{\circ}C$, M_s is determined to be $\sim$765 emu/cm^3, which is close to the reported value of $\sim$780 emu/cm^3 in bulk samples.[18,24]

To use the Co_2MnGa film as a spin current source and reduce the required net current for the SOT effect, we also grew thinner, 10 nm films of Co_2MnGa on MgO (100) substrate following the conditions for samples A and C using the aforementioned techniques. We choose to employ samples grown at 400 °C for the following study as 10 nm films grown at temperatures higher than 500 °C show discontinuities; meanwhile, from the discussion before, we would expect substantial $L2_1$ phase to exist in $T_{dep} = 400\,^{\circ}C$ samples. The two 10 nm films were also characterized with VSM as shown in Fig. 2(b), where a trend similar to the 100 nm ones was observed, with M_s $\sim$ 590 emu/cm^3 for the high temperature grown film. The difference from bulk magnetization for thin samples has been reported in the literature and attributed to strain-induced changed in the electronic structure or a slight off-stoichiometric composition.[21,22] Atomic force microscopy (AFM) was employed to further examine the surface morphology for the 10 nm samples, and a smooth surface with an RMS roughness of 0.18 nm is obtained [Fig. 1(d)].

It has been shown previously that due to the Berry curvatures from the Weyl points or nodal lines, the $L2_1$-ordered Co_2MnGa exhibit much stronger AHE compared with the chemically disordered phases. We then measured the Hall resistivity by applying a magnetic field, H_z, normal to the film (xy) plane, and measuring the voltage transverse to the current. Empirically, the Hall resistivity (ρ_{yx}) in a ferromagnetic material is given by $\rho_{yx} = R_o H_z + \rho_{AH}$, where R_o is the ordinary Hall coefficient, H_z is the applied field, and ρ_{AH} is the anomalous Hall resistivity. By subtracting the contribution from the ordinary Hall effect (<1%), we obtained results for ρ_{AH} for 100 and 10 nm films, respectively [Figs. 2(c) and 2(d)]. A similar trend of monotonic increase in ρ_{AH} with the increase in T_{dep} was observed for both set of films. The maximum absolute value of ρ_{AH} in the $L2_1$-ordered Co_2MnGa (100 nm) film at $T_{dep} = 600\,^{\circ}C$ is $\sim$14.6 $\mu\Omega$ cm, comparable to the experimental value in bulk Co_2MnGa.[18] For the 10 nm samples, the ρ_{AH} is 0.98 and 5.4 $\mu\Omega$ cm for RT and $T_{dep} = 400\,^{\circ}C$ samples, respectively. We note that a sharp decrease in the ρ_{AH} with thicknesses below 20 nm has been studied elsewhere and is attributed to the reduction in majority spin contribution to the Berry curvature as well as an increase in the extrinsic scattering mechanism (side-jump or skew scattering) as the surface effects become more prominent.[22,26,27]

To unravel the spin-current generation efficiency from the spin Hall effect (SHE) with different degrees of chemical ordering, we grow

multilayer stacks of Co_2MnGa (10 nm)/Cu (1 nm)/Co_xTb_{1-x} (7 nm)/Ru (3 nm) using magnetron sputtering. The Co_2MnGa film employed in the two samples correspond to the growth and annealing condition of samples A and C in Table I, separately. For the high temperature sample, following the *in situ* annealing, we allow the samples to cool to room temperature preceding the Cu/CoTb/Ru growth within the same growth chamber. The transition metal-rare earth alloy, Co_xTb_{1-x}, is a ferrimagnetic with robust bulk perpendicular magnetic anisotropy (PMA) whose anisotropy and magnetization can be adjusted by tuning chemical compositions.[28,29] We co-sputtered these films using cobalt and terbium targets and chose a 7 nm film with an atomic ratio of $Co_{0.87}Tb_{0.13}$ to get optimal PMA for the stack. To avoid direct exchange coupling between Co_2MnGa and CoTb, we insert a 1 nm copper spacer layer for its long spin diffusion length and negligible SHE.[30,31] Finally, the stack is capped with a thin ruthenium layer to prevent oxidation of CoTb.

The magnetic hysteresis loops in both in-plane and out-of-plane orientation for RT and 400 °C sample are shown in Figs. 3(a) and 3(c), respectively. Consistent with our results above, we see a larger in-plane saturation magnetic moment for $T_{dep} = 400$ °C sample as compared to RT grown one. From the out-of-plane MH curve, we see relatively sharp switching edges from the PMA CoTb layers. We note that the CoTb film grown on 400 °C Co_2MnGa exhibits a weaker, less steeper switching compared with the one grown on the RT sample, likely due to the different textures of the underlying film which influences the PMA of CoTb through crystallization. Meanwhile, the different seeding layer also led to different magnetic moment in the CoTb layer, as shown in Figs. 3(a) and 3(c), although the chemical composition of the two CoTb layers is nominally the same. We then patterned these films into Hall bar structures for transport measurements. The anomalous Hall resistance (R_H) as a function of out-of-plane magnetic field for both sets of samples is shown in Figs. 3(b) and 3(d). Comparing the R_H loop with the MH loop, we can identify the sharp edges as being the contributions from the AHE of the PMA CoTb, and the linear slope as being caused by the Co_2MnGa film which has a hard axis along the out-of-plane direction. We also note that the linear part of the R_H signal has a larger slope for high temperature sample [Fig. 3(d)] as compared to room temperature sample [Fig. 3(b)], consistent with our results for bare Co_2MnGa samples [Fig. 2(d)].

By monitoring the change in the switching curves of the CoTb layer under applied current, we are able to quantitatively determine the SOT exerted from the Co_2MnGa film onto CoTb. Here, we adapted the SOT magnetometry technique from Pai *et al.*,[32] where a constant in-plane bias field, H_x, is applied along the current (I_{dc}) direction, and the lateral shift in the R_H vs H_z curve is measured for a series of applied I_{dc}. This overall shift of the hysteresis loop is due to the

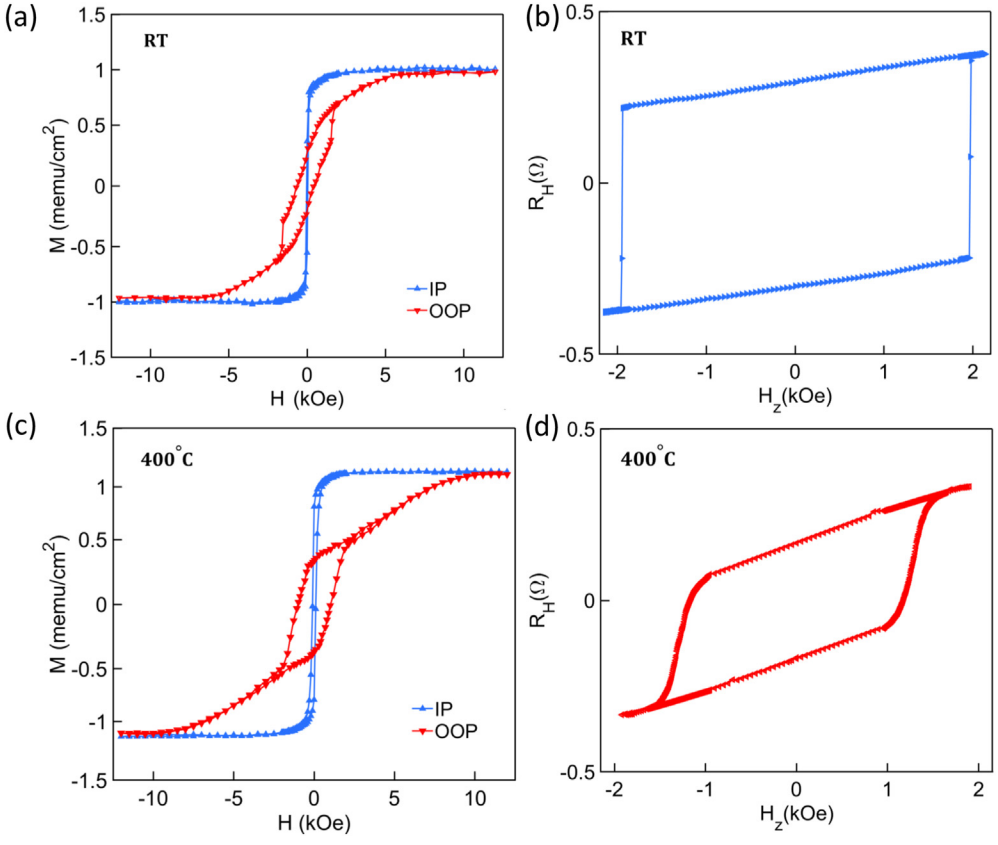

FIG. 3. In plane and out-of-plane magnetic hysteresis loops of the heterostructure $Co_2MnGa/Cu/Co_{0.87}Tb_{0.13}/Ru$ for (a) T_{dep} = RT and (c) $T_{dep} = 400$ °C samples. The anomalous Hall resistance as a function of applied out-of-plane field H_z for the stack atop (b) T_{dep} = RT and (d) $T_{dep} = 400$ °C.

Slonczewski (damping-like) torque which manifests as an out-of-plane effective field, H_z^{eff}, during the switching process. The experimental setup is schematically shown in Fig. 4(a). As shown in Figs. 4(b) and 4(c), the loop center deviates from zero in opposite directions for $\pm I_{dc}$ due to this SOT effective field (H_z^{eff}) from Co_2MnGa. The current induced H_z^{eff}, as a function of the current density in the Co_2MnGa layer (J_e), is plotted in Figs. 5(a) and 5(b) for room temperature and 400 °C samples, separately. Here, we calculate H_z^{eff} using the differential value under positive and negative current $H_{eff}^{z} = \frac{H_o(I_{dc}) - H_o(-I_{dc})}{2}$, where H_o is the center of hysteresis loop for $\pm I_{dc}$, to get rid of zero point offset of the magnetic field from the magnet. The ratio of H_z^{eff} and the applied current density j_e, defined as $\chi \equiv H_z^{\text{eff}}/j_e$ then gives the damping-like SOT efficiency. The sign of this slope χ changes as the domain wall moment in the Neél-type walls realign parallel to the applied in-plane field, $\pm H_x$,[32] as observed in our plots [Figs. 5(a) and 5(b)]. Also, in both samples, we see no noticeable shifting of curves at $H_x = 0$ as expected. In Figs. 5(c) and 5(d), we summarize the measured χ as a function of $\pm H_x$. For the RT grown sample, we see that the slope of H_x vs χ curve deviates from a linear curve between 500 and 610 Oe [Fig. 5(c)], suggesting that the external field approaches the Dzyaloshinskii–Moriya interaction field (H_{DMI}), and χ measured under the highest H_x approximately reflects its saturation value χ_{sat}. For the $T_{dep} = 400$ °C, we see a smaller deviation from the linear slop slope at $H_x \sim \pm 610$ Oe, indicating that a larger H_x is required to completely overcome H_{DMI} [Fig. 5(d)]. The effective spin Hall angle α_{SH} is related to χ_{sat} through[32]

$$\alpha_{SH} = \frac{2}{\pi}\frac{2e\mu_0\chi^{sat}M_s\,t}{\hbar}, \quad (1)$$

where $\hbar$ is the reduced Planck's constant, e is the electron charge, μ_0 is the vacuum permeability, and M_s and $t = 7$ nm are the saturation magnetization and the thickness of the CoTb layer, respectively. Using the saturation magnetization of CoTb ($M_s \sim 383$ emu/cc) grown on the RT Co_2MnGa sample and the measured $\chi^{sat} \approx 2.5 \times 10^{-6}$ Oe A^{-1} cm^2, α_{SH} is determined to be -11.8%. We note that the sign of α_{SH} is consistent with and its magnitude is comparable to the recent results on $B2$-ordered Co_2MnGa (001).[24] Because of the limitation in the in-plane field capability of our instrument, we did not achieve full saturation χ^{sat} for the 400 °C sample. However, we can still estimate a lower bound based on the results we have. Using the M_s of CoTb ($\sim$495 emu/cm^3) grown on the 400 °C sample and assuming that $\chi^{sat} \approx 0.78 \times 10^{-6}$ Oe A^{-1} cm^2, we get -5.2% as the lower bound on effective spin Hall angle.

It has been shown both theoretically and experimentally that the large intrinsic AHE in Co_2MnGa arises from the large Berry curvature. Considering the very similar intrinsic and extrinsic scattering mechanisms driving AHE and SHE and similar scaling relationship, Co_2MnGa is conceived as a possible candidate for reaching a large spin Hall angle. Furthermore, it has been shown theoretically that a strong intrinsic SHE can be realized in Weyl semimetals,[33,34] as supported by the recent experimental determination of spin Hall angle of ~ -0.19 $L2_1$ Co_2MnGa.[25] However, in our measurement, we do not see the obvious advantage in the chemically ordered sample over the disordered one. Within our measured field range, the disordered B2 phase sample even shows a larger spin–orbit torque efficiency compared with the $L2_1$ phase sample. More theoretical calculations focused on the relationship between the spin Hall effect and the chemical ordering can potentially help in solving this puzzle. Moreover, this observation may be related to the following extrinsic reasons. First, it is possible that the surface quality of the Co_2MnGa film with high growth and annealing temperature is not as transparent as the RT one for reaching an optimal spin-mixing conductance, which will decrease the measured SOT efficiency. Second, as mentioned earlier, the sharp decrease in AHE attributed to the reduction in majority spin contribution to the Berry curvature can also potentially explain the smaller than expected values of α_{SH} for very thin films used in our case. Future experiments with thicker Co_2MnGa ($t > 20$ nm) layers will be useful for verifying this point. Finally, the in-plane field used in our experiment was barely enough to reach the SOT efficiency saturation, suggesting a very strong Dzyaloshinskii–Moriya interaction (DMI) in the $L2_1$ Co_2MnGa/Cu/CoTb system. Further experiments with higher in-plane field can pinpoint the exact value of the spin Hall angle and lead to better understanding of enhanced DMI.

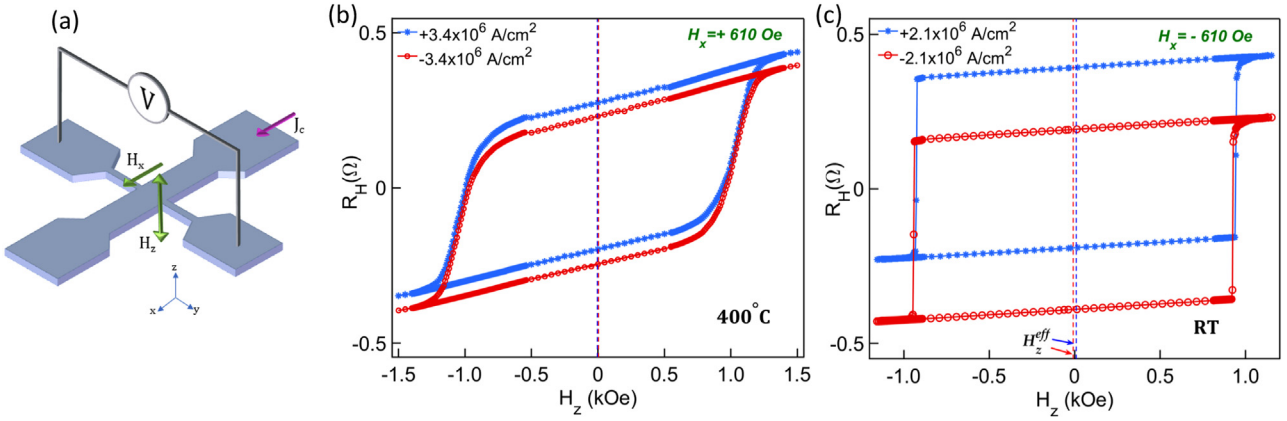

FIG. 4. (a) Schematic of experimental geometry of SOT magnetometry. The width and length of the Hall bar are 8 and 40 μm, respectively. (b) R_H vs H_z for a 400 °C sample, the dc current density is $\pm 3.4 \times 10^6$ A/cm^2 through Co_2MnGa, and the applied bias field is $H_x = +610$ Oe. (c) R_H vs H_z for the Co_2MnGa grown at room temperature with a current density of $\pm 2.1 \times 10^6$ A/cm^2 and a bias field $H_x = -610$ Oe. Slight vertical offsets are introduced for $\pm I_{dc}$ loops in (b) and (c) for clarity.

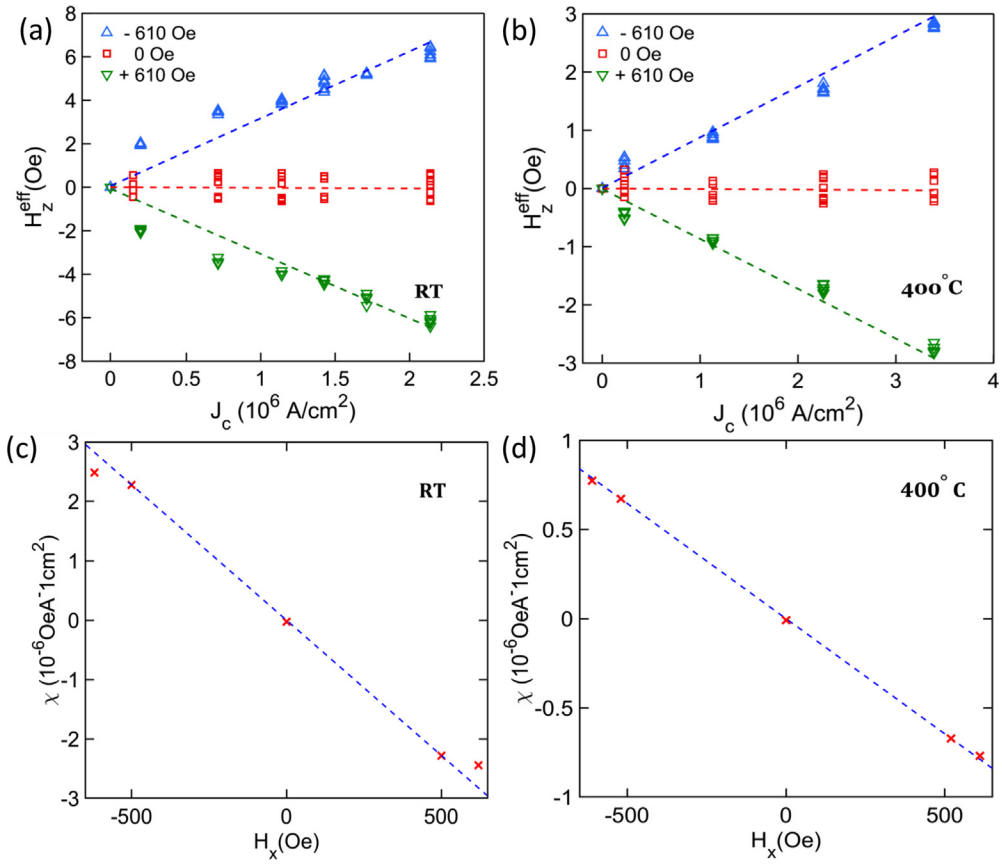

FIG. 5. Calibration of the SOT efficiency in the Co_2MnGa_{Tdep}/Cu/CoTb samples. The center shift field H_{eff}^z as a function of applied current density for (a) T_{dep} = RT and (b) T_{dep} = 400 °C samples. The dotted lines are a linear fit to the experimental data points. The slope of these lines, χ, gives the damping-like SOT efficiency plotted in (c) for T_{dep} = RT and (d) T_{dep} = 400 °C samples as a function of in-plane field H_x.

In conclusion, we have grown epitaxial MWSM Co_2MnGa thin films with different chemical orderings. Consistent with the previous reports, we have shown a monotonic decrease in saturation magnetization, M_s, as well as the anomalous Hall resistivity from $L2_1$-ordered to $B2$ Co_2MnGa films. In addition, we have shown the generation of SOTs from Co_2MnGa with different crystalline phases. Within our experimental accuracy, we do not observe a strong advantage of the $L2_1$-ordered sample over the $B2$ phase in the efficiency of SOT. Further studies on the spin transparencies across the Co_2MnGa/magnetic free layer interfaces as well as other extrinsic mechanisms' contributions to SOT in Co_2MnGa are needed to reveal the full picture of the promised Berry curvature driven charge to spin conversions in MWSM.

This work was supported by the National Science Foundation under Award No. DMR-2104912 and the Semiconductor Research Corporation.

AUTHOR DECLARATIONS

Conflict of Interest

The authors have no conflicts to disclose.

Author Contributions

Taqiyyah S. Safi: Conceptualization (equal); Formal analysis (lead); Investigation (lead); Project administration (equal); Validation (lead); Visualization (lead); Writing – original draft (lead); Writing – review & editing (equal). **Chung-Tao Chou:** Investigation (supporting); Writing – review & editing (supporting). **Justin T Hou:** Investigation (supporting); Writing – review & editing (supporting). **Jiahao Han:** Investigation (supporting); Writing – review & editing (supporting). **Luqiao Liu:** Conceptualization (equal); Funding acquisition (lead); Project administration (equal); Supervision (lead); Writing – review & editing (equal).

DATA AVAILABILITY

The data that support the findings of this study are available from the corresponding author upon reasonable request.

REFERENCES

[1]S. M. Huang, S. Y. Xu, I. Belopolski *et al.*, "A Weyl Fermion semimetal with surface Fermi arcs in the transition metal monopnictide TaAs class," Nat. Commun. **6**, 7373 (2015).
[2]B. Q. Lv, H. Weng, B. B. Fu *et al.*, "Experimental discovery of Weyl semimetal TaAs," Phys. Rev. X **5**, 031013 (2015).

[3]S.-Y. Xu, I. Belopolski, N. Alidoust *et al.*, "Discovery of a Weyl fermion semimetal and topological Fermi arcs," Science **349**, 613 (2015).
[4]L. Yang, Z. Liu, Y. Sun *et al.*, "Weyl semimetal phase in the noncentrosymmetric compound TaAs," Nat. Phys. **11**, 728–732 (2015).
[5]B. Yan and C. Felser, "Topological materials: Weyl semimetals," Annu. Rev. Condens. Matter Phys. **8**, 337–354 (2017).
[6]X. Huang, L. Zhao, Y. Long *et al.*, "Observation of the chiral-anomaly-induced negative magnetoresistance in 3D Weyl semimetal TaAs," Phys. Rev. X **5**, 031023 (2015).
[7]C. L. Zhang, S. Y. Xu, I. Belopolski *et al.*, "Signatures of the Adler–Bell–Jackiw chiral anomaly in a Weyl fermion semimetal," Nat. Commun. **7**, 10735 (2016).
[8]C. Shekhar, A. Nayak, Y. Sun *et al.*, "Extremely large magnetoresistance and ultrahigh mobility in the topological Weyl semimetal candidate NbP," Nat. Phys. **11**, 645–649 (2015).
[9]S. A. Parameswaran, T. Grover, D. A. Abanin *et al.*, "Probing the chiral anomaly with nonlocal transport in three-dimensional topological semimetals," Phys. Rev. X **4**, 031035 (2014).
[10]Y. Baum, E. Berg, S. A. Parameswaran, and A. Stern, "Current at a distance and resonant transparency in Weyl semimetals," Phys. Rev. X **5**, 041046 (2015).
[11]M. Ikhlas, T. Tomita, T. Koretsune *et al.*, "Large anomalous Nernst effect at room temperature in a chiral antiferromagnet," Nat. Phys. **13**, 1085–1090 (2017).
[12]T. Matsuda, N. Kanda, T. Higo *et al.*, "Room-temperature terahertz anomalous Hall effect in Weyl antiferromagnet Mn_3Sn thin films," Nat. Commun. **11**, 909 (2020).
[13]S. Nakatsuji, N. Kiyohara, and T. Higo, "Large anomalous Hall effect in a non-collinear antiferromagnet at room temperature," Nature **527**, 212–215 (2015).
[14]Y. Okamura, S. Minami, Y. Kato *et al.*, "Giant magneto-optical responses in magnetic Weyl semimetal $Co_3Sn_2S_2$," Nat. Commun. **11**, 4619 (2020).
[15]P. Li, J. Koo, W. Ning *et al.*, "Giant room temperature anomalous Hall effect and tunable topology in a ferromagnetic topological semimetal Co_2MnAl," Nat. Commun. **11**, 3476 (2020).
[16]E. Liu, Y. Sun, N. Kumar *et al.*, "Giant anomalous Hall effect in a ferromagnetic kagome-lattice semimetal," Nat. Phys. **14**, 1125–1131 (2018).
[17]Q. Wang, Y. Xu, R. Lou *et al.*, "Large intrinsic anomalous Hall effect in half-metallic ferromagnet $Co_3Sn_2S_2$ with magnetic Weyl fermions," Nat. Commun. **9**, 3681 (2018).
[18]A. Sakai, Y. P. Mizuta, A. A. Nugroho *et al.*, "Giant anomalous Nernst effect and quantum-critical scaling in a ferromagnetic semimetal," Nat. Phys. **14**, 1119–1124 (2018).
[19]V. A. Oksenenkoa, V. A. Kulagin, Y. V. Kudryavtsev *et al.*, "Magnetic properties of Co_2MnGa Heusler alloy films with different crystalline order," J. Magn. Magn. Mater. **316**(2), e407–e410 (2007).
[20]Q. Wang, Z. Wen, T. Kubota, T. Seki, and K. Takanashi, "Structural-order dependence of anomalous Hall effect in Co_2MnGa topological semimetal thin films," Appl. Phys. Lett. **115**, 252401 (2019).
[21]Z. Zhu, T. Higo, S. Nakatsuji, and Y. Otani, "Magnetic and transport properties of amorphous, *B*2 and $L2_1$ Co_2MnGa thin films," AIP Adv. **10**, 085020 (2020).
[22]A. Markou, D. Kriegner, J. Gayles *et al.*, "Thickness dependence of the anomalous Hall effect in thin films of the topological semimetal Co_2MnGa," Phys. Rev. B **100**, 054422 (2019).
[23]P. Swekis, A. S. Sukhanov, Y. Chen *et al.*, "Magnetic and electronic properties of Weyl semimetal Co_2MnGa thin films," Nanomaterials **11**, 251 (2021).
[24]K. Tang, Z. Wen, Y. Lau *et al.*, "Magnetization switching induced by spin–orbit torque from Co_2MnGa magnetic Weyl semimetal thin films," Appl. Phys. Lett. **118**, 062402 (2021).
[25]L. Leiva, S. Granville, Y. Zhang *et al.*, "Giant spin Hall angle in the Heusler alloy Weyl ferromagnet Co_2MnGa," Phys. Rev. B. **103**, L041114 (2021).
[26]B. Ludbrook, B. Ruck, and S. Granville, "Perpendicular magnetic anisotropy in Co_2MnGa and its anomalous Hall effect," Appl. Phys. Lett. **110**, 062408 (2017).
[27]Y. Zhang, Y. Yin, G. Dubuis *et al.*, "Berry curvature origin of the thickness-dependent anomalous Hall effect in a ferromagnetic Weyl semimetal," npj Quantum Mater. **6**, 17 (2021).
[28]J. Finley and L. Liu, "Spin-orbit-torque efficiency in compensated ferrimagnetic cobalt-terbium alloys," Phys. Rev. Appl. **6**, 054001 (2016).
[29]P. Hansen, C. Clausen, G. Much, M. Rosenkranz, and K. Witter, "Magnetic and magneto-optical properties of rare-earth transition-metal alloys containing Gd, Tb, Fe, Co," J. Appl. Phys. **66**, 756 (1989).
[30]J. Bass and W. P. Pratt, "Spin-diffusion lengths in metals and alloys, and spin-flipping at metal/metal interfaces: An experimentalist's critical review," J. Phys.: Condens. Matter **19**, 183201 (2007).
[31]H. L. Wang, C. H. Du, Y. Pu *et al.*, "Scaling of spin Hall angle in 3d, 4d, and 5d metals from $Y_3Fe_5O_{12}$/metal spin pumping," Phys. Rev. Lett. **112**, 197201 (2014).
[32]C. F. Pai, M. Mann, A. J. Tan, and G. S. D. Beach, "Determination of spin torque efficiencies in heterostructures with perpendicular magnetic anisotropy," Phys. Rev. B **93**, 144409 (2016).
[33]Y. Sun, Y. Zhang, C. Felser, and B. Yan, "Strong intrinsic spin Hall effect in the TaAs family of Weyl semimetals," Phys. Rev. Lett. **117**, 146403 (2016).
[34]J.-C. Tung and G.-Y. Guo, "High spin polarization of the anomalous Hall current in Co-based Heusler compounds," New J. Phys. **15**, 033014 (2013).